2013-03-26

Geomorphological mapping with a small unmanned aircraft system (sUAS): feature detection and accuracy assessment of a photogrammetrically-derived digital terrain model

Hugenholtz, Chris H.

Elsevier

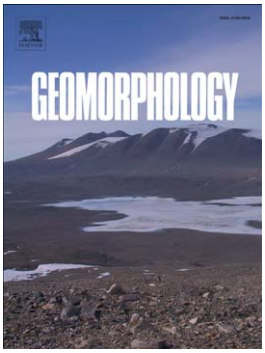

Geomorphological mapping with a small unmanned aircraft system (sUAS): Feature detection and accuracy assessment of a photogrammetrically-derived digital terrain model

Chris H. Hugenholtz, Ken Whitehead, Owen W. Brown, Thomas E. Barchyn, Brian J. Moorman, Adam LeClair, Kevin Riddell, Tayler Hamilton

PII: S0169-555X(13)00173-6
DOI: doi: 10.1016/j.geomorph.2013.03.023
Reference: GEOMOR 4298

To appear in: *Geomorphology*

Received date: 31 August 2012
Revised date: 18 March 2013
Accepted date: 26 March 2013

Please cite this article as: Hugenholtz, Chris H., Whitehead, Ken, Brown, Owen W., Barchyn, Thomas E., Moorman, Brian J., LeClair, Adam, Riddell, Kevin, Hamilton, Tayler, Geomorphological mapping with a small unmanned aircraft system (sUAS): Feature detection and accuracy assessment of a photogrammetrically-derived digital terrain model, *Geomorphology* (2013), doi: 10.1016/j.geomorph.2013.03.023

Geomorphological mapping with a small unmanned aircraft system (sUAS): feature detection and accuracy assessment of a photogrammetrically-derived digital terrain model

Chris H. Hugenholtz[a,b], Ken Whitehead[b,c], Owen W. Brown[a], Thomas E. Barchyn[a], Brian J. Moorman[b], Adam LeClair[b], Kevin Riddell[a], Tayler Hamilton[a]

[a] Department of Geography, University of Lethbridge, 4401 University Drive, Lethbridge, Alberta, Canada, T1K 3M4.

[b] Department of Geography, University of Calgary, 2500 University Drive NW, Calgary, Alberta, Canada, T2N 1N4.

[c] Accuas Inc., 450 Lakeshore Dr. NE, Box 97 Salmon Arm, British Columbia, Canada, V1E 4N2.

*Corresponding author. Tel: +1-403-220-3374, Fax: +1-403-282-6561.

E-mail address: chhugenh@ucalgary.ca (C.H. Hugenholtz)

Highlights:

- In 4.5 hours we collected airborne imagery and ground data to produce a 1 m DTM
- The accuracy of the sUAS DTM is equivalent to a bare Earth LiDAR DTM
- Small-scale biogeomorphic features in 0.1 m imagery were not visible in 1 m imagery

Abstract. Small unmanned aircraft systems (sUAS) are a relatively new type of aerial platform for acquiring high-resolution remote sensing measurements of Earth surface processes and landforms. However, despite growing application there has been little quantitative assessment of sUAS performance. Here we present results from a field experiment designed to evaluate the accuracy of a photogrammetrically-derived digital terrain model (DTM) developed from imagery acquired with a low-cost digital camera onboard an sUAS. We also show the utility of the high-resolution (0.1 m) sUAS imagery for resolving small-scale biogeomorphic features. The experiment was conducted in an area with active and stabilized aeolian landforms in the southern Canadian Prairies. Images were acquired with a Hawkeye RQ-84Z Aerohawk fixed-wing sUAS. A total of 280 images were acquired along 14 flight lines, covering an area of 1.95 km^2. The survey was completed in 4.5 hours, including GPS surveying, sUAS setup and flight time. Standard image processing and photogrammetric techniques were used to produce a 1 m resolution DTM and a 0.1 m resolution orthorectified image mosaic. The latter revealed previously un-mapped bioturbation features. The vertical accuracy of the DTM was evaluated with 99 Real-Time Kinematic GPS points, while 20 of these points were used to quantify horizontal accuracy. The horizontal root mean squared error (*RMSE*) of the orthoimage was 0.18 m, while the vertical *RMSE* of the DTM was 0.29 m, which is equivalent to the *RMSE* of a bare earth LiDAR DTM for the same site. The combined error from both datasets was used to define a threshold of the minimum elevation difference that could be reliably attributed to erosion or deposition in the seven years separating the sUAS and LiDAR datasets. Overall, our results suggest that sUAS-acquired imagery may provide a low-cost, rapid, and flexible alternative to airborne LiDAR for geomorphological mapping.

Key words: Small unmanned aircraft system (sUAS); Digital terrain model accuracy; LiDAR; High-resolution geomorphic mapping; Topographic change detection.

1. Introduction

Measurement and analysis of Earth surface morphology and morphodynamics are fundamental tenets of geomorphology. Increasing availability and access to digital topographic data over the past few decades has steadily improved the quantitative rigor of our discipline (e.g., Zhou et al., 2008; Smith and Pain, 2009; Tarolli et al., 2009), spurred progress in geomorphometry (Hengl and Reuter, 2009), and expanded the role of geomorphology within the broader Earth surface science community (e.g., Murray et al., 2009). New methods of acquiring topographic data with a high spatial resolution (e.g., LiDAR) have not only exposed greater detail about landforms and landscape morphology, but have also provided opportunities to match the scale of topographic data with the spatio-temporal scale of the geomorphological features or processes under investigation (e.g., Nield et al., 2011). Several clearinghouses of digital topographic data with common formats and free access have also come online recently (e.g., National Center for Airborne Laser Mapping, http://ncalm.org and United States Geological Survey's Earth Resources Observation and Science Center, http://eros.usgs.gov). By making topographic data available and standardized (e.g., Slatton et al., 2007), these initiatives act as catalysts for many disciplines of Earth surface research (cf. Murray et al., 2009) and clearly demonstrate the utility of high resolution remote sensing data.

LiDAR data, whether acquired from airborne, mobile, or *in situ* platforms, are steadily becoming the preferred source for measurements of topography. LiDAR (Light Detection and

Ranging) is an active remote sensing technology where millions of laser pulses are reflected off target surfaces and the position of each recorded reflection is calculated in 3D space, producing what is referred to as a 'point cloud'. Point clouds are commonly simplified to a raster grid for analysis of landscape topography. LiDAR data typically have higher spatial resolution than most conventional methods (i.e., total station, GPS, photogrammetry and InSAR) and can penetrate through vegetation canopies to measure ground surface elevation. From airborne and mobile platforms LiDAR data can be acquired over large areas in considerably less time than conventional ground-based survey techniques (e.g., total station and GPS); however, cost is a limiting factor for operationalizing LiDAR in many geomorphology research programs (Slatton et al., 2007). For many researchers the availability of LiDAR data (previously collected for some other purpose) governs study site choice as on-demand LiDAR surveys are often too expensive for most research budgets (although this may be changing). *In situ* LiDAR, known as terrestrial laser scanning (TLS), is a more affordable alternative to airborne LiDAR with greater operational flexibility as TLS units are typically mounted on tripods. However, this vantage point limits TLS data to a much smaller areal extent, which may not be suitable for certain studies. Considering these challenges, an alternative method is desirable, if it could inexpensively provide data with high spatial resolution, reasonable coverage, and greater operational flexibility than airborne LiDAR.

Digital photogrammetry is an alternative to LiDAR that is steadily decreasing in cost due to the proliferation of inexpensive cameras, diverse aerial platforms, and online computer vision software such as structure from motion (SfM) and multiview stereo (MVS) (e.g., James and Robson, 2012; Westoby et al., 2012; Fonstad et al., in press). Conventional applications of photogrammetry in geomorphology mainly involved piloted aircraft, but a number of other

platforms have been tested, including balloons (Boike and Yoshikawa, 2003), kites (Marzolff and Poesen, 2009), telescoping masts (Hauet et al., 2009), and small unmanned helicopters (Niethammer et al., 2010). The latter platform is particularly noteworthy because it affords a level of automation to the aerial survey that has been difficult to achieve with other methods.

In this paper we evaluate a new approach for high definition topographic mapping involving a small unmanned aircraft system (sUAS). Small UASs (< 25 kg) are a type of powered aircraft that evolved from radio-controlled (RC) and military 'drone' aircraft. These aircraft are also commonly referred to as unmanned/uninhabited aerial vehicles (UAVs) or remotely-piloted aircraft (RPA). They have integrated autopilot technology, which gives them semi- or fully-autonomous navigation, flight control and image acquisition capabilities. Remote sensing with sUASs is growing rapidly (Dunford et al., 2009; Rango et al., 2009; Jaakkola et al., 2010; Lin et al., 2011; Stefanik et al., 2011; Hugenholtz et al., 2012a); thus, the goal of this study is to test the accuracy of these data. We developed a high-resolution (1 m) digital terrain model (DTM) produced photogrammetrically from overlapping images acquired by an sUAS at a field site with sand dunes in Canada. The total cost of the sUAS, including all the components and the base station, was approximately $30,000 CAD, which is comparatively less expensive than airborne and terrestrial LiDAR systems. We tested the accuracy of the DTM with independently collected GPS check points. Results show that the vertical error of the sUAS DTM is equivalent to the error of a LiDAR bare Earth DTM acquired in 2005. These results are encouraging for sUAS applications in geomorphology that involve topographic mapping and morphodynamic measurements.

2. Study site

The experiment was conducted in the Bigstick Sand Hills of southwest Saskatchewan, Canada (Fig. 1). This site was chosen because airborne LiDAR data were previously acquired here in 2005 as part of a regional environmental study (Great Sand Hills Scientific Advisory Committee, 2007), thus providing a frame of reference for assessing the accuracy of the sUAS DTM. Morphological changes of parabolic dunes and blowout hollows at this site over the previous few decades are described by Hugenholtz and Wolfe (2006, 2009) and Hugenholtz et al. (2008, 2009). Larger-scale topography underlying the dunes is glaciogenic (mostly moraine) emplaced during recession of the Laurentide Ice Sheet. Dune stabilization has progressed over the past 200 years in this area; active barchan dunes have transformed into vegetated parabolic dunes (Wolfe and Hugenholtz, 2009). Periodic disturbances of vegetation on stabilized dunes have led to the development of blowout hollows on some dunes within of the study area.

The site is located in the dry mixed grassland ecoregion and contains a heterogeneous mix of vegetation types. The most extensive plants on the sparsely-vegetated dunes are *Psoralea lanceolata* and *Rumex venosus*, which are rhizomatous pioneer species tolerant to minor deposition. Stabilized dunes and interdunes also contain *Rosa woodsii*, *Agropyron dasystachyum*, *Koeleria macrantha*, and *Stipa comata*. Shrubs and trees are also found in interdunes (e.g., *Elaeagnus commutate*, *Salix* spp., *Populus tremuloides*). As will be shown in the imagery, small mounds from northern pocket gophers (*Thomomys talpoides*) and other fossorial mammals give rise to a heterogeneous distribution of bare and vegetated surfaces on stabilized dunes and interdunes. Additional features on the landscape include trails from cattle, and gravel trails for vehicle access to natural gas wells.

3. Methodology

3.1. Aerial survey and image processing

The sUAS survey was conducted on 30 June 2012. The time required to complete the aerial survey was about 4.5 hours, which included sUAS setup, deployment of ground control targets, GPS surveying, and flying time. The aircraft used was a Hawkeye RQ-84Z Aerohawk. This is a small, fixed wing UAS, measuring 1.4 m long with a 2.9 m wind span (Fig. 2). It weighs less than 6.2 kg and can fly up to 2 hours on lithium-ion polymer batteries. The aircraft is hand-launched and is capable of parachute or skid landing, depending on terrain and land cover. Aviation regulations in Canada dictate that UASs must be operated within visual line of sight during the survey, which limits coverage to approximately 1 km distance from the central ground station. The Aerohawk uses an autopilot manufactured by Micropilot®. Color (i.e., RGB) images were acquired with an Olympus PEN Mini E-PM1 camera (14–42 mm lens). Prior to the survey the exposure of the camera was calibrated with a light meter over bare sand. No internal camera calibration was performed prior to the survey.

Weather conditions during the aerial survey were ideal. Hourly wind speed measured at a weather station 25 km to the southwest was 2.5 m s^{-1} at 10 m above ground surface. Wind direction was easterly. There was 0% cloud cover and the air temperature was 25°C. Collectively, these conditions ensured the aircraft was stable during flight and that lighting conditions were consistent for all 280 images.

Prior to the survey a fly file was generated which contains information to guide the aircraft autonomously during the flight. The fly file is created with third party software and requires information about the total area of the survey, flying height, aircraft speed, and desired image overlap. These parameters were set to 1.92 km^2, 200 m height, 10 m s^{-1}, and 65% overlap, respectively. This yielded 14 flight lines, 280 image waypoints, and a total flying time of 50

minutes (although only half of the 280 images were used in the final processing). To avoid crabbing, which is the angling of the aircraft nose due to crosswind, the flight lines were oriented east–west (Fig. 3). After the hand-launch take-off the aircraft operated autonomously for the entire duration of the flight, acquiring images at the pre-defined waypoints and returning to the take-off site at the end of the survey. The aircraft was monitored continuously from the ground station, which consisted of a laptop running flight control software and an antenna. For landing, a servo onboard the aircraft was triggered from the ground station in order to deploy the parachute. Fig. 3 shows an overview of the survey design, including the positions of flight lines, image waypoints, ground control points (GCPs), and GPS test points.

During the survey the autopilot recorded aircraft parameters continuously and stored these data in a flight log that was downloaded after landing. The flight log was used to provide an initial estimate of the image centre positions and the ω, φ, and κ rotation parameters, corresponding to the roll, pitch, and yaw of the aircraft, respectively. These parameters were used to set up a project using Trimble's Inpho photogrammetric processing software. Ground control points (GCPs) were used to improve the accuracy of triangulation. In total, 28 GCPs were surveyed using a Trimble R7 real-time kinematic (RTK) GPS system (Fig. 3). The GCPs were 0.6 m yellow squares located throughout the site and clearly visible from images.

The triangulation was run twice for all images. For the first run, all 28 GCPs were used to obtain the best overall accuracy. The camera calibration was then modified to minimize the residuals. Inpho software allows optimization of an existing camera calibration via a computed correction grid. Once the best possible camera calibration had been achieved, the images were reinitialised. Every second GCP was then changed to an independent check point. The ground coordinates of these points were calculated through the triangulation process but played no part

in the determination of the triangulation parameters. They thus provided an independent check on the accuracy of triangulation.

Following triangulation, a digital surface model (DSM) and a digital terrain model (DTM) were generated for the site. A DSM provides a detailed surface for the entire area; however it includes all vegetation and extraneous features, which are not normally wanted in a survey. A DTM provides a filtered representation of the terrain without vegetation. To produce a DTM, Inpho uses a feature-based matching technique, hierarchically applied to a series of image pyramids. A robust surface is then generated using finite element analysis. This means that surface interpolation is based on a comparatively widely-spaced grid, which has the effect of filtering out most minor terrain variations resulting from vegetation. For the DSM Inpho uses an extremely dense grid of irregular surface points and carries out image-matching for all possible image pairs. This produces multiple solutions for the same image points, and robust filtering is used to identify the strongest possible match. Because of the much higher density of points used in surface creation, a DSM is much more sensitive to the effects of vegetation and minor surface variations. Both the DTM and DSM algorithms are matching points to the top of the vegetation layer. However because of the wider spacing between intermediate points in the processing, the sensitivity of a DTM to vegetation is reduced. Conversely, a DSM will normally provide better results in areas of low texture, such as exposed sand. Both techniques are therefore useful. For our case study a composite model was produced at 1 m spatial resolution, with the DTM being used for most of the area and the DSM filling in details in locally steep areas missed by the DTM. This composite model was used to orthorectify the input images and to provide a series of orthoimages with a spatial resolution of 0.1 m. Finally, the orthoimages were mosaiced to produce a seamless colour-balanced image of the entire study site.

3.2. DTM accuracy assessment

The vertical accuracy of the sUAS-acquired DTM was assessed in two ways. First, a total of 99 test points were acquired with the RTK GPS. The points were distributed on flat to gentle slopes in the area around the active dunes (Fig. 3). The number of GPS test points (n) was determined from the following:

$$n = \left(\frac{z_{\alpha/2} \cdot \sigma}{E}\right)^2 \quad (1)$$

where $z_{\alpha/2}$ is the critical *z*-value, σ is the standard deviation and E is the margin of error. For our case study we assumed the following criteria: $z_{\alpha/2}$ = 1.645 (90% confidence level), σ = 0.3 m and E = 0.05 m. This yields a sample size of 98 or more. The average horizontal and vertical errors of the GPS measurements were 0.009 and 0.013 m, respectively.

To quantify the error we measured the vertical difference between the elevation of each GPS test point and the elevation of the DTM grid cell at the point. We then calculated the root mean square error of elevation ($RMSE_z$), which measures the dispersion of the frequency distribution of deviations between the GPS elevation and the DTM elevation, expressed as:

$$RMSE_z = \sqrt{\frac{1}{n}\sum_{i=1}^{n}(z_{\mathrm{d}i} - z_{\mathrm{r}i})^2} \quad (2)$$

where $z_{\mathrm{d}i}$ is the *i*-th elevation value measured on the DTM surface, $z_{\mathrm{r}i}$ is the corresponding elevation measured by GPS, and n is the total number of elevation points checked. Second, we

calculated the elevation difference between the sUAS DTM and the LiDAR bare Earth DTM acquired in 2005. If the two DTMs were perfectly matched, there would be no difference between them, with the exception of active (unvegetated) areas of dunes and blowouts subject to aeolian erosion and deposition in the seven years between the two datasets. Flight parameters of the airborne LiDAR data are reported in Brown and Hugenholtz (2011).

4. Results

4.1. Accuracy assessment

The 0.1 m orthorectified image mosaic produced from the 140 images is shown in Fig. 4. From the 99 GPS test points, 20 points were used to determine the horizontal *RMSE* of the orthoimagery. These points correspond to features easily resolved in the imagery (mostly the centers of pocket gopher mounds). The resulting horizontal *RMSE* is 0.18 m, which is almost double the image resolution. However, compared to other remote sensing data, this is a relatively small horizontal error, especially when considering the large number of images (n = 140) used to create the orthoimage.

According to the 99 GPS test points, $RMSE_z$ of the sUAS DTM is 0.29 m, which is the same as $RMSE_z$ for the LiDAR DTM. Histograms in Fig. 5 also show that the distribution of the vertical difference between the 99 GPS elevations and the corresponding DTM elevations is similar in both datasets, although there is a slightly larger error range for the LiDAR DTM. Both histograms are approximately normally distributed. In the histograms positive values indicate that the elevations of points on the DTM surface are greater than the corresponding elevations of GPS points. The mean, median and standard deviation of the elevation difference between the sUAS DTM and the GPS points are 0.14, 0.07, and 0.26 m, respectively. The mean, median and

standard deviation of the elevation difference between the LiDAR DTM and the GPS points are 0.05, 0.03, and 0.29 m, respectively. The maximum absolute error of the sUAS DTM is 0.76 m, while for the LiDAR DTM it is 1.06 m. The majority of difference values in the sUAS DTM are positive (72%) with elevations greater than the corresponding GPS elevations, whereas in the LiDAR DTM the total is 58%. This suggests that the elevations of cells in the sUAS DTM frequently lie above the actual ground surface elevation. We interpret this offset as an effect caused by the vegetation. Overall, this analysis shows that the vertical error of the sUAS DTM is comparable to the LiDAR DTM.

By combining the error of the two datasets we can estimate the lower limit of topographic change that can be attributed to erosion and deposition during the seven years between the LiDAR and sUAS surveys. We adopt a simplified approach to define this limit or threshold (*T*):

$$T = \pm 3 \times \sqrt{(RMSE_{\text{LiDAR}})^2 + (RMSE_{\text{sUAS}})^2} \quad (3)$$

where the multiplier, 3, represents the extreme tails of a normal probability distribution. From Eq. (3) the resulting threshold value is ±1.23 m, which means that any elevation difference between −1.23 m and +1.23 m is most likely a result of error, whereas differences exceeding this threshold are more likely to represent real topographic changes associated with erosion and deposition.

Fig. 6 shows the two DTMs and the corresponding difference map produced by subtracting the LiDAR DTM from the sUAS DTM. The difference map encompasses a smaller area because the photogrammetric modeling of the sUAS imagery yielded some visually discernible errors, including one dune in the southeast corner that is completely missing in the

sUAS DTM (Fig. 6B). Although both DTMs show comparable levels of morphological detail, the difference map shows some systematic differences, particularly on the windward (west-facing) slopes. In these areas difference values are dominantly positive (white in the map), which suggests deposition. However, most of these slopes are covered by vegetation and face the dominant wind direction, which would typically result in erosion if they were devoid of vegetation. We therefore interpret that many of these areas represent error. However, on the active dunes and blowouts there are some areas of erosion on west-facing slopes and deposition on nearby east- and northeast-facing slopes that are real. By using the threshold value calculated from Eq. (3) we can calculate the total area with difference values below or above the cutoff. In Fig. 6D we superimposed these areas onto the orthoimage. From this approach we estimate that 99.3% of the total area is within the threshold, while 0.7% lies outside it. The latter translates into a total area of 6.67×10^3 m^2 that has undergone erosion or deposition. We note that the amount of erosion in some areas is comparable to values reported by Hugenholtz (2010) at a nearby parabolic dune with blowouts.

A histogram showing the distribution of the elevation difference between the two DTMs is presented in Fig. 7. The histogram is approximately normally distributed with a mean, median and standard deviation of 0.07, 0.08, and 0.51 m, respectively. Excluding the active landforms, 80% of cells from stable parts of the landscape have an absolute vertical difference of 0.3 m, while 1% exceeds 1m.

4.2. Feature detection

While the primary goal of this study was to assess the vertical accuracy of the sUAS DTM, we noted several prominent features in the orthorectified imagery that were not obvious in

previous RGB imagery collected during the airborne LiDAR survey in 2005. The first is sparse vegetation on the dunes and blowouts (Fig. 8). The ability to resolve sparse vegetation on dunes with remote sensing is a challenge in aeolian geomorphology (Hugenholtz et al., 2012b). It is not only important in terms of quantifying the aeolian sediment transport rate (Lancaster and Baas, 1998), but also in the context of assessing dune stabilization and allied effects on species that rely on sparsely-vegetated dune habitat, such as the endangered Ord's kangaroo rat (*Dipodomys ordii*). Previous work at this site involved crude field-based estimates of vegetation cover in order to map the presence of sparse vegetation at relative coarse timescales (Hugenholtz, 2010); however, the high spatial resolution of the sUAS imagery makes it possible to use image classificaton techniques in order to map and ultimately monitor the dune vegetation cover (Fig. 8B), potentially improving the quantitative understanding of dune stabilization. This is especially important for parameterizing and testing numerical models of vegetated dune morphodynamics (e.g., Durán and Herrmann, 2006; Barchyn and Hugenholtz, 2012a,b).

The second notable observation from the 0.1 m orthorectified imagery is the extent of biogeomophic features across the study site (Fig. 9A). Small bright patches occur throughout the study area and correspond to the activities of fossorial mammals (e.g., *Thomomys talpoides*). Prior to this imagery the pervasiveness of these features across the landscape was unknown; however, the sUAS imagery clearly shows that they are widespread, and as such, they represent a major form of disturbance and bioturbation affecting soil development and plant succession (cf Butler and Butler, 2009; Knight, 2009). Differences in the brightness of mounds appear to be caused by aging, such that older mounds are darker due to increased vegetation cover and litter accumulation, whereas younger mounds are largely devoid of litter and have very little vegetation. The ability to visually discriminate mounds in conventional imagery with 1 m

resolution is limited because most mounds are typically less than 1 m in width (Fig. 8B). Although new mounds developed in the 7-year timespan between the images, they have always been a prominent feature across this landscape, so their absence throughout most of the image in Fig. 9B is solely due to the coarser image resolution. Although it is possible to detect some mounds in 1 m imagery, they can only be detected if they are larger than individual pixels, or if a series of mounds are inter-connected.

5. Discussion and conclusions

In this work, a small unmanned aircraft system (sUAS) was used to create a high resolution orthoimage and a digital terrain model of an aeolian landscape. Small UASs are a relatively new type of remote sensing platform that have distinct advantages over conventional piloted aircraft and satellites, notably their low cost and operational flexibility. The scale and type of sUAS image data can be tailored to match the scale of geomorphic processes and landforms under investigation. This remains a major issue in geomorphology; most researchers are forced to adapt to the spatial and temporal resolution of available remote sensing data. Small UASs are also far more flexible; for example, our experiment was completed in ~4.5 hours and from the data acquired in that timeframe we were able to produce a 0.1 m orthorectified image mosaic and a 1 m DTM. Similar resolution is not straightforward to obtain with conventional remote sensing platforms. In order to acquire a DTM with comparable areal extent and resolution (1 m) from field-based measurements with an RTK GPS, we estimate the survey would require up to several weeks or months to complete.

Despite the clear operational advantages of sUASs for geomorphological research, our results show that the vertical accuracy of these data requires further consideration, especially in

the context of quantifying landscape erosion and deposition processes. While the vertical accuracy of the sUAS DTM is on par with the LiDAR DTM at this site, the amount of combined error adds a lot of uncertainty to change detection and the resulting volume calculations with these data. We surmise that vegetation is one of several key sources of error in the sUAS DTM because the elevations of points of the sUAS DTM were frequently higher than the corresponding GPS points. LiDAR is inherently better suited for geomorphological applications in vegetated environments than photogrammetrically-derived DTMs because laser pulses from LiDAR can penetrate vegetation canopies to produce a bare earth DTM, whereas photogrammetric DTMs include vegetation, which requires filtering. Mini LiDARs are being developed for sUAS platforms to help mitigate this problem (see Jaakkola et al., 2010; Lin et al., 2011), but at present, photogrammetrically-derived DTMs from sUAS platforms are most applicable for topographic mapping in environments with minimal surface vegetation. We anticipate, therefore, that more accurate DTMs could be produced at sites with minimal vegetation cover, like desert dunes, glaciers and river channels.

Another source of error in the sUAS data comes from the platform, which, because of its lightweight, is inherently less stable than larger piloted aircraft. The instability of the platform changes the roll, pitch, and yaw of the aircraft during flight, and this can affect the accuracy of the DTM and orthorectified image mosaic. Although most photogrammetric software can compensate for this distortion, it can contribute to error in matching the exact centre of targets in overlapping images. Compounding the error potentially arising from aircraft instability is the error associated with the use of an uncalibrated digital camera. By determining the principal distance, principal offset point and lens distortion parameters, it may be possible to improve the accuracy of subsequent sUAS DTMs. However, we hypothesize that vegetation effects will still

result in a systematic over-estimation of ground surface elevation compared to the bare Earth LiDAR DTM and GPS points. Further experimentation is required to separate the contributions from all possible sources of error.

In conclusion, our study provides a preliminary assessment of the capabilities of an sUAS for topographic mapping and geomorphic feature detection. We find that the horizontal error of an orthorectified image mosaic produced with 140 images was 0.18 m, which is greater than the image resolution, but also much smaller than conventional imagery from piloted aircraft and satellite imagery. The vertical accuracy of the sUAS DTM was equivalent to that of a LiDAR bare earth DTM, but the amount of error may be reduced by improving aircraft stability and camera calibration. Further research is required in order to increase the vertical accuracy of sUAS DTMs so that they can be used to measure topographic changes associated with landform morphodynamics. In our view, this has the potential to transform many geomorphology research topics.

Acknowledgements

This research was supported by funding to CHH from Cenovus Energy, the Natural Sciences and Engineering Research Council of Canada, and Alberta Innovates. We thank Peter Pachmann (Accuas Inc.) for field assistance during the aerial survey. We also thank the Editor and two anonymous reviewers for their comments and suggestions.

References

Barchyn, T.E., Hugenholtz, C.H., 2012a. Aeolian dune field geomorphology modulates the stabilization rate imposed by climate. Journal of Geophysical Research – Earth Surface 117, F02035. doi:10.1029/2011JF002274.

Barchyn, T.E., Hugenholtz, C.H., 2012b. A process-based hypothesis for the barchan-parabolic transformation and implications for dune activity modeling. Earth Surface Processes and Landforms 37, 1456-1462.

Boike, J., Yoshikawa, K., 2003. Mapping of periglacial geomorphology using kite/balloon aerial photography. Permafrost and Periglacial Processes 14, 81-85.

Brown, O.W., Hugenholtz, C.H., 2011. Estimating aerodynamic roughness (z_0) in a mixed prairie grassland with airborne LiDAR. Canadian Journal of Remote Sensing 37, 422-428.

Butler, D.R., Butler, W.D., 2009. The geomorphic effects of gophers on soil characteristics and sediment compaction: a case study from alpine treeline, Sangre de Cristo Mountains, Colorado, USA. The Open Geology Journal 3, 82-89.

Dunford, R., Michel, K., Gagnage, M., Piégay, H., Trémelo, M.–L., 2009. Potential and constraints of unmanned aerial vehicle technology for the characterization of Mediterranean riparian forest. International Journal of Remote Sensing 30, 4915-4935.

Durán, O., Herrmann, H.J., 2006. Vegetation against dune mobility. Physical Review Letters 97, 188001. doi: 10.1103/PhysRevLett.97.188001.

Fonstad, M.A., Dietrich, J.T., Courville, B.C., Jensen, J.L., Carbonneau, P.E., in press. Topographic structure from motion: a new development in photogrammetric measurement. Earth Surface Processes and Landforms. doi: 10.1002/esp.3366.

Great Sand Hills Scientific Advisory Committee, 2007. Great Sand Hills Regional Environmental Study. Government of Saskatchewan, 233 p.

Hauet, A., Muste, M., Ho, H.-C., 2009. Digital mapping of riverine waterway hydrodynamic and geomorphic features. Earth Surface Processes and Landforms 34, 242-252.

Hengl, T., Reuter, H.I., 2009. Geomorphometry: Concepts, Software, Applications. Elsevier, Amsterdam.

Hugenholtz, C.H., 2010. Topographic changes of a supply-limited inland parabolic sand dune during the incipient phase of stabilization. Earth Surface Processes and Landforms 35, 1674-1681.

Hugenholtz, C.H., Wolfe, S.A., 2006. Climate controls and morphodynamics of two aeolian blowouts on the northern Great Plains, Canada. Earth Surface Processes and Landforms 31, 1540-1557.

Hugenholtz, C.H., Wolfe, S.A., 2009. Form-flow interactions in an aeolian saucer blowout. Earth Surface Processes and Landforms 34, 919-928.

Hugenholtz, C.H., Wolfe, S.A., Moorman, B.J., 2008. Effects of local sediment supply on the morphodynamics and stratigraphy of active parabolic dunes, Saskatchewan, Canada. Canadian Journal of Earth Sciences 45, 321-335.

Hugenholtz, C.H., Wolfe, S.A., Walker, I.J., Moorman, B.J., 2009. Spatial and temporal patterns of sediment transport across an inland parabolic dune, Bigstick Sand Hills, Saskatchewan, Canada. Geomorphology 105, 158-170.

Hugenholtz, C.H., Moorman, B.J., Riddell, K., Whitehead, K., 2012a. Small unmanned aircraft systems (sUAS) for remote sensing. EOS 93(25), 236-237.

Hugenholtz, C.H., Levin, N., Barchyn, T.E., Baddock, M., 2012b. Remote sensing and spatial analysis of aeolian sand dunes: a review and outlook. Earth-Science Reviews 111, 319-334.

Jaakkola, A., Hyyppä, J., Kukko, A., Yu, X., Kaartinen, H., Lehtomäki, M., Lin, Y., 2010. A low-cost multi-sensoral mobile mapping system and its feasibility for tree measurements. ISPRS Journal of Photogrammetry and Remote Sensing 65, 514-522.

James, M.R., Robson, S., 2012. Straightforward reconstruction of 3D surfaces and topography with a camera: accuracy and geosciences application. Journal of Geophysical Research – Earth Surface 117, F03017. doi: 10.1029/2011JF002289.

Knight, J., 2009. Infilled pocket gopher tunnels: seasonal features of high alpine plateau. Earth Surface Processes and Landforms 34, 590-595.

Lin, Y., Hyyppä, J., Jaakkola, A., 2011. Mini-UAV-borne LiDAR for fine-scale mapping, IEEE Geoscience and Remote Sensing Letters 8, 426-430. doi: 10.1109/LGRS.2010.2079913.

Lancaster, N., Baas, A.C.W., 1998. Influence of vegetation cover on sand transport by wind: field studies at Owens Lake, California. Earth Surface Processes and Landforms 23, 69-82.

Marzolff, I., Poesen, J., 2009. The potential of 3D gully monitoring with GIS using high-resolution aerial photography and a digital photogrammetry system. Geomorphology 111, 48-60.

Murray, A.B., Lazarus, E., Ashton, A., Baas, A.C.W., Coco, G., Coulthard, T., Fonstad, M., Haff, P., McNamara, D., Paola, C., Pelletier, J., Reinhardt, L., 2009. Geomorphology, complexity, and the emerging science of the Earth's surface. Geomorphology 103, 496–505.

Nield, J.M., Wiggs, G.F.S., Squirrell, R.S., 2011. Aeolian sand strip mobility and protodune development on a drying beach: examining surface moisture and surface roughness patterns measured by terrestrial laser scanning. Earth Surface Processes and Landforms 36, 513-522.

Niethammer, U., Rothmund, S., James, M.R., Travelletti, J., Joswig, M., 2010. UAV-based remote sensing of landslides, International Archives of Photogrammetry, Remote Sensing Spatial Infoation Science 38, 496–501.

Rango, A., Herrick, J.E., Havstad, K., Browning, D., 2009. Unmanned aerial vehicle-based remote sensing for rangeland assessment, monitoring, and management. Journal of Applied Remote Sensing 3, 033542. doi: 10.1117/1.321682.

Slatton. K.C., Carter. W.E., Shrestha, R.L., Dietrich, W., 2007. Airborne Laser Swath Mapping: achieving the resolution and accuracy required for geosurficial research. Geophysical Research Letters 34, L23S10. doi:10.1029/2007GL031939.

Smith, M.J., Pain, C.F., 2009. Applications of remote sensing in geomorphology. Progress in Physical Geography 33, 568-582.

Stefanik, K.V., Gassaway, J.C., Kochersberger, K., Abbott, A.L., 2011. UAV-based stereo vision for rapid aerial terrain mapping. GIScience & Remote Sensing 1, 24-49.

Tarolli, P., Arrowsmith, J.R., Vivoni, E.R., 2009. Understanding Earth surface processes from remotely sensed digital terrain models. Geomorphology 113, 1-3.

Westoby, M.J., Brasington, J., Glasser, N.F., Hambrey, M.J., Reynolds, J.M., 2012. 'Structure-from-Motion' photogrammetry: a low-cost, effective tool for geosciences applications. Geomorphology 179, 300-314.

Wolfe, S.A., Hugenholtz, C.H., 2009. Canadian prairie barchan dune fields stabilized under recent climate warming. Geology 37, 1039-1042.

Zhou, Q,, Lees, B., Tang, G., 2008. Advances in Digital Terrain Analysis. Springer-Verlag, Berlin.

Figure captions

Fig. 1. Map showing the location of the study site (star) in the southwest corner of the Province of Saskatchewan (50° 11' 10.07" N, 109° 11' 47.63" W).

Fig. 2. The Hawkeye RQ-84Z Aerohawk fixed-wing UAS. Some of the key features of the Aerohawk are shown in A), including the parachute and pitot tube. B) View of the aircraft midflight showing the camera turret.

Fig. 3. Overview of the survey design, including: image waypoints along the seven flight lines, the locations of the 25 GCPs, and the 99 GPS test points. Note that while 14 flight lines were flown, only seven (140 images) were used to create the orthoimage and the DTM. The background image is from Google™ Earth.

Fig. 4. Orthorectified image mosaic with 0.1 m ground resolution. The locations and spatial extents of Figs. 8 and 9 are indicated by small boxes. The UTM (12N) coordinates are in meters.

Fig. 5. Histograms of the vertical difference between the GPS test points and the sUAS DTM (A) and the LiDAR DTM (B).

Fig. 6. Comparison of the sUAS DTM (A) and LiDAR DTM (B). Subtraction of A) from B) yields the difference map in C). Black and white polygons superimposed on the orthoimage in D) correspond to regions with erosion (black) and deposition (white) that exceed the error threshold calculated from Eq. (2) (±1.23 m). The UTM (12N) coordinates are in meters.

Fig. 7. Histogram showing the elevation difference between the UAS DTM and the LiDAR DTM.

Fig. 8. High resolution UAS imagery makes it possible to detect and map sparse vegetation on sand dunes. A) UAS imagery. B) Results of a maximum likelihood supervised classification applied to the area shown in A). White represents bare sand, while black represents vegetation. C) Circular quadrat with a diameter of 0.83 m, showing sparse vegetation (*Psoralea lanceolata* and *Rumex venosus*). The small circle in image in A) corresponds to the image in C).

Fig. 9. A comparison of (A) the 0.1 m sUAS imagery and (B) a standard 1 m aerial photograph collected during the 2005 LiDAR survey (B). Pocket gopher mounds (bright areas) are pervasive in the sUAS imagery, but obscured in the 1 m aerial photograph. One of the yellow GCP targets (0.6×0.6 m) is shown in the southeast corner of image (A).

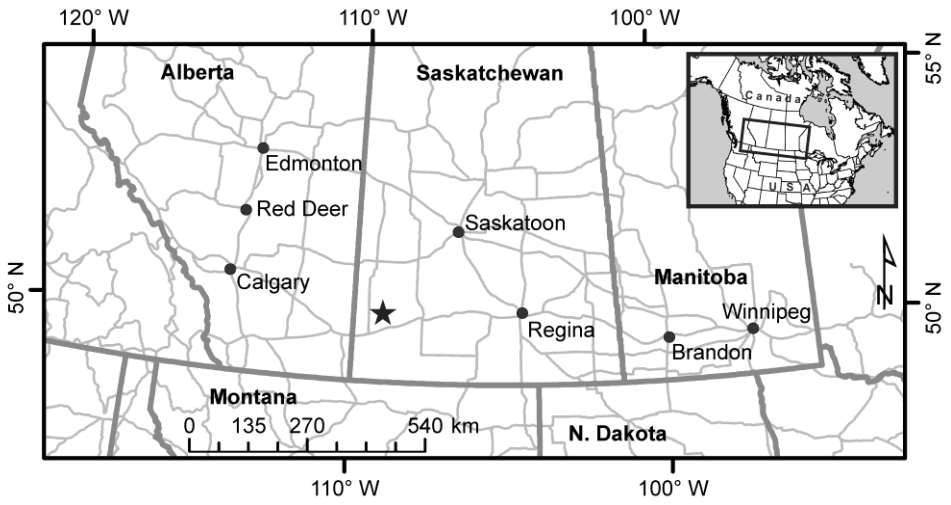

Fig. 1

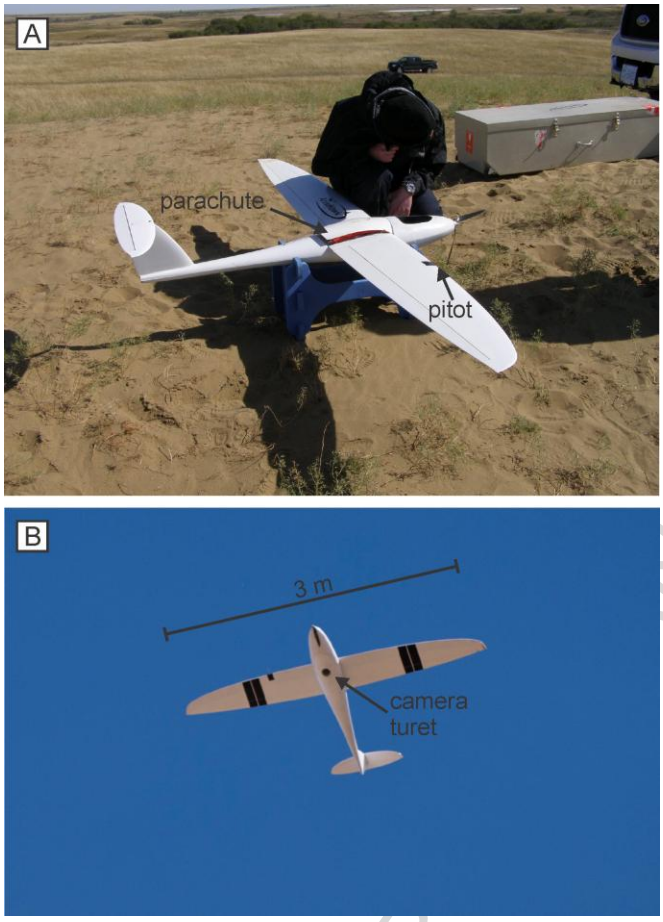

Fig. 2

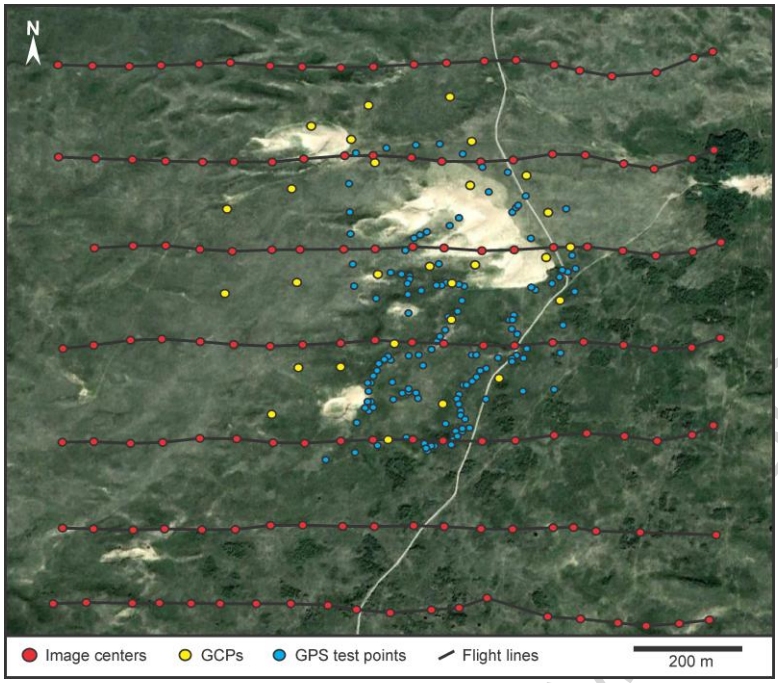

Fig. 3

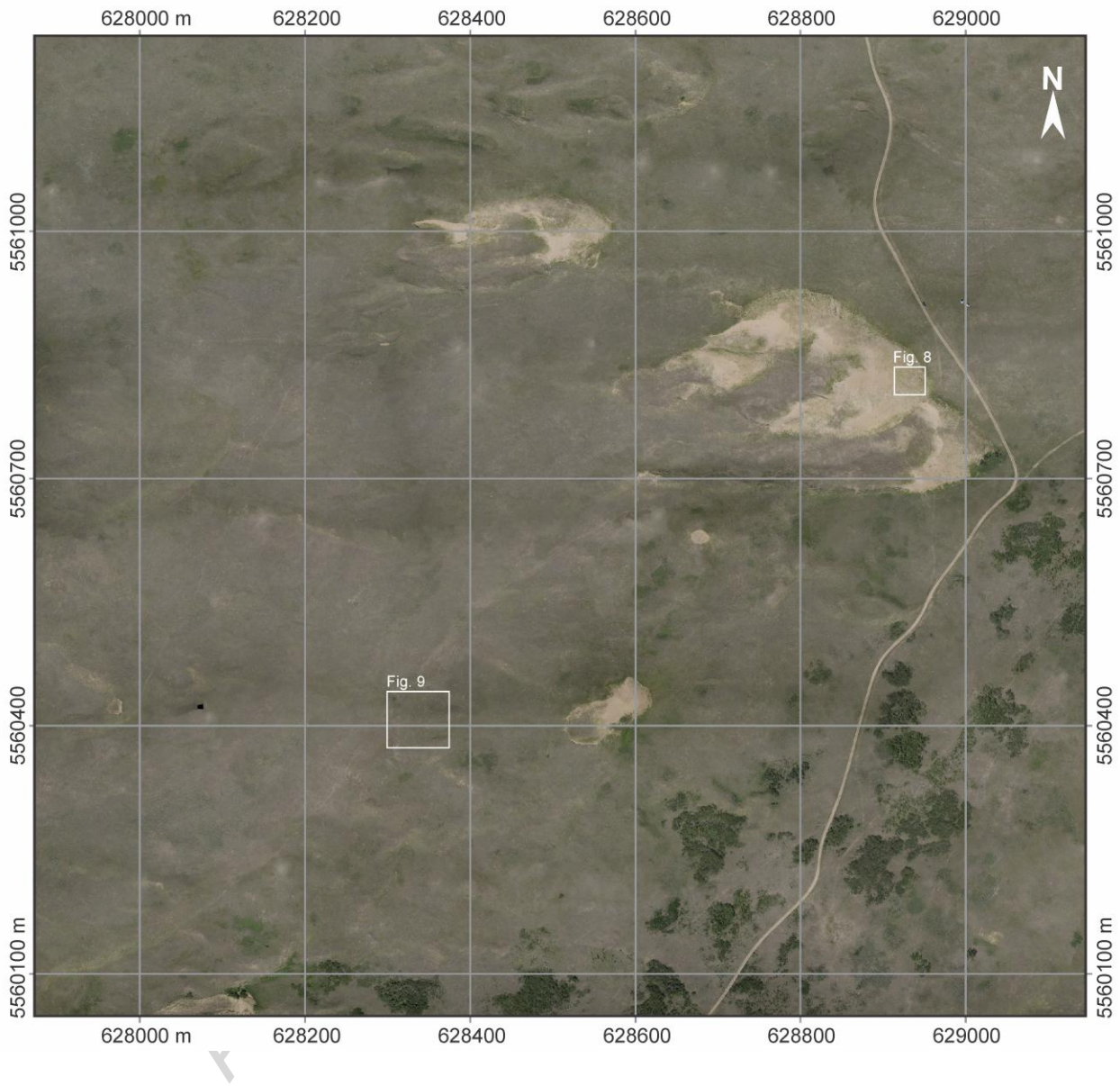

Fig. 4

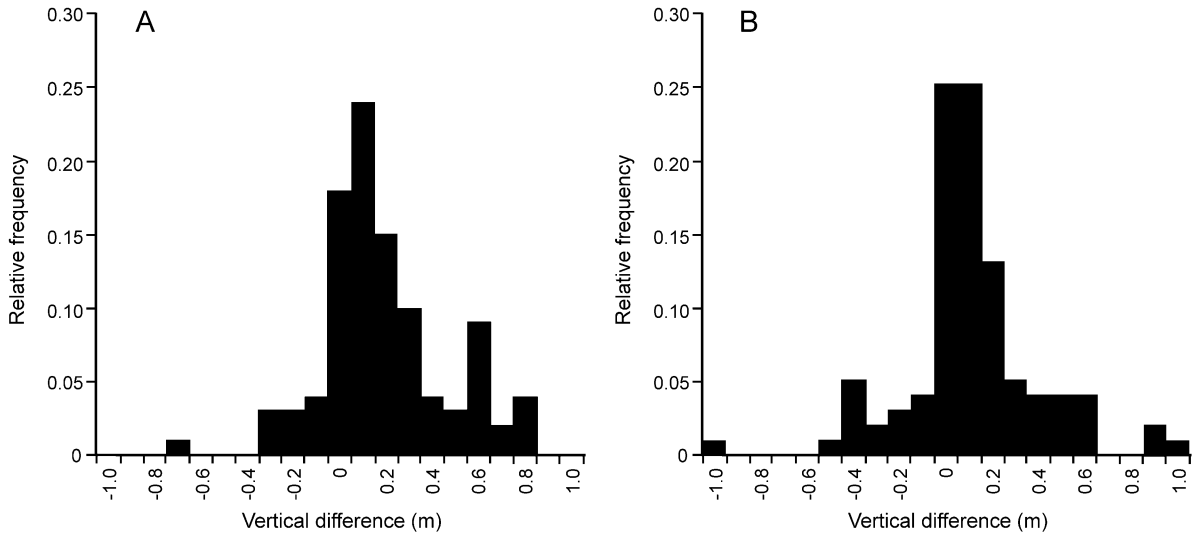

Fig. 5

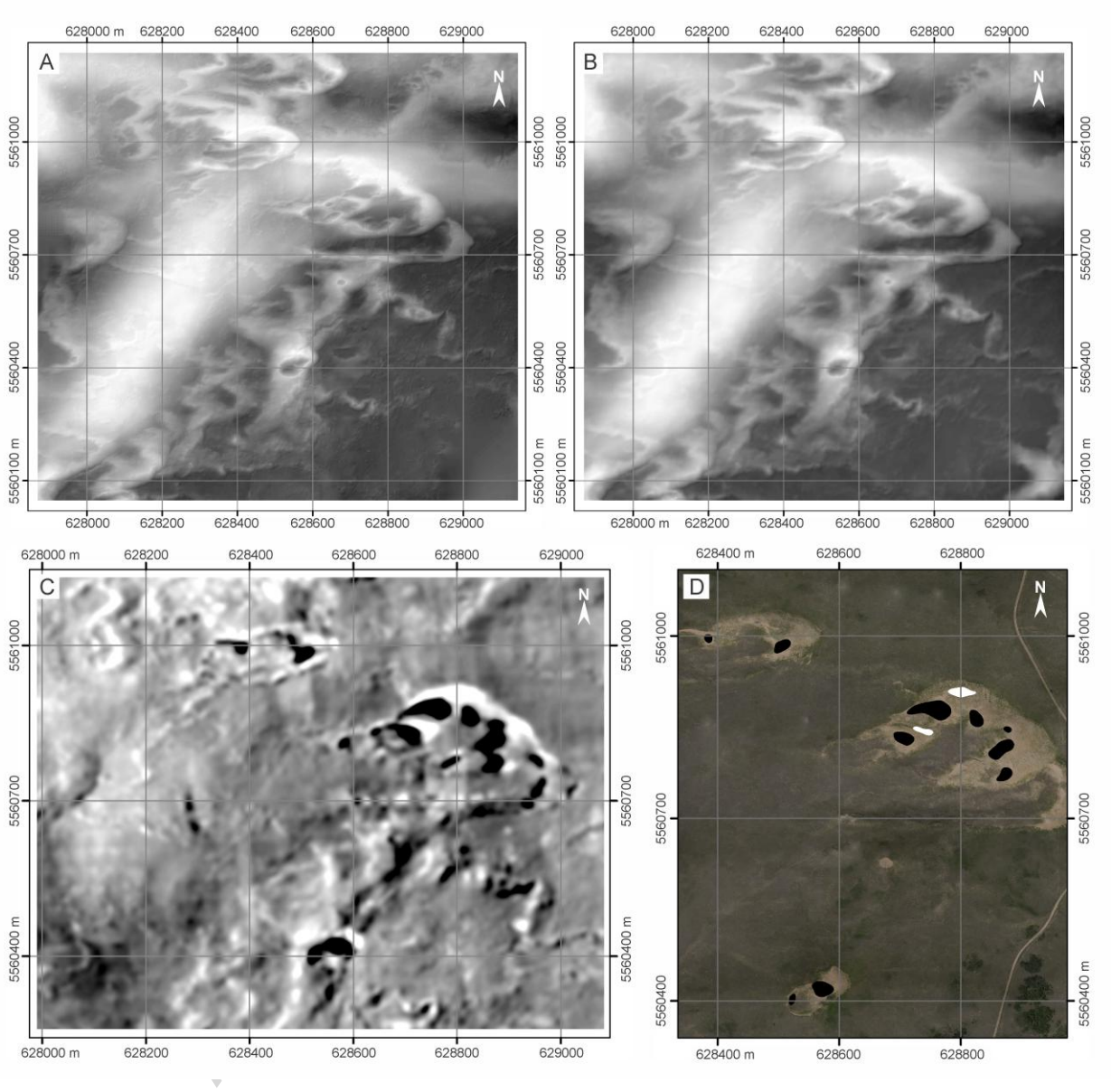

Fig. 6

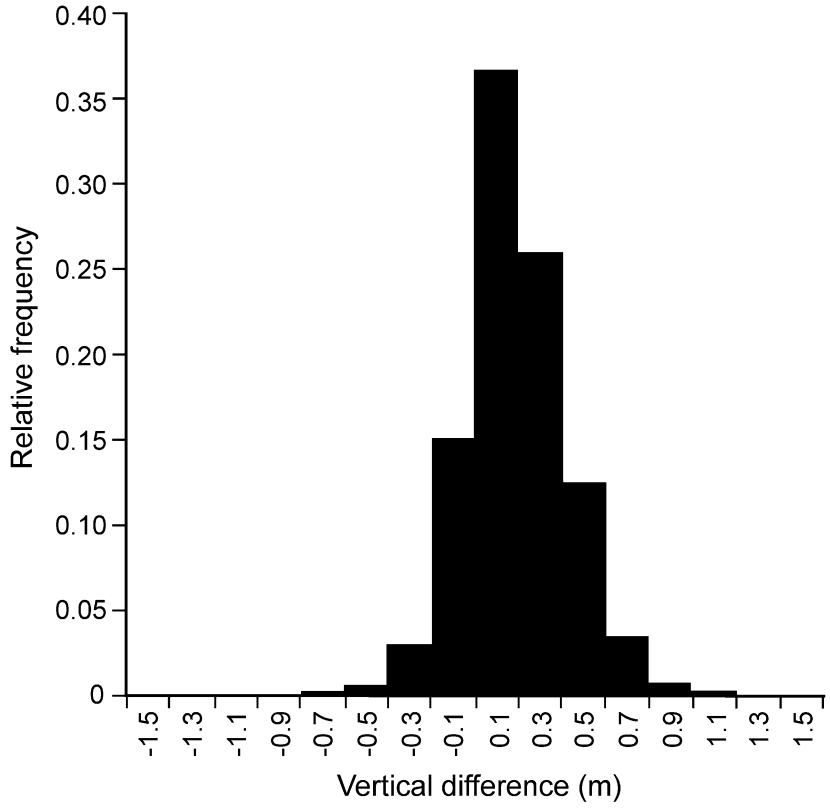

Fig. 7

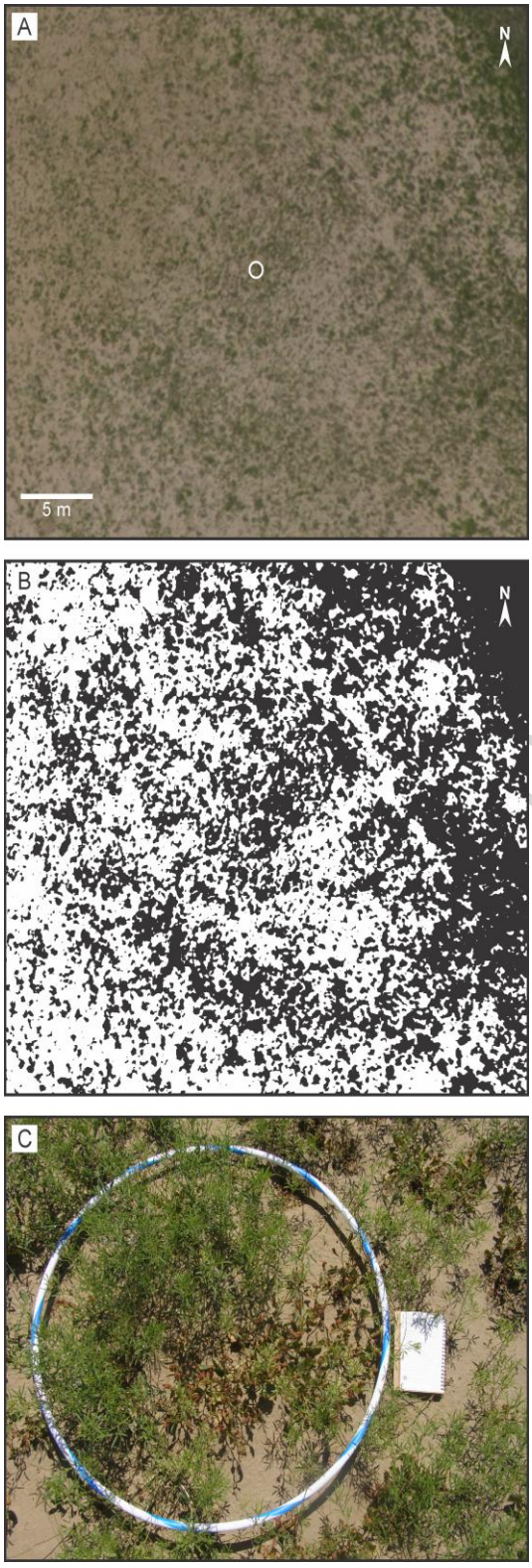

Fig. 8

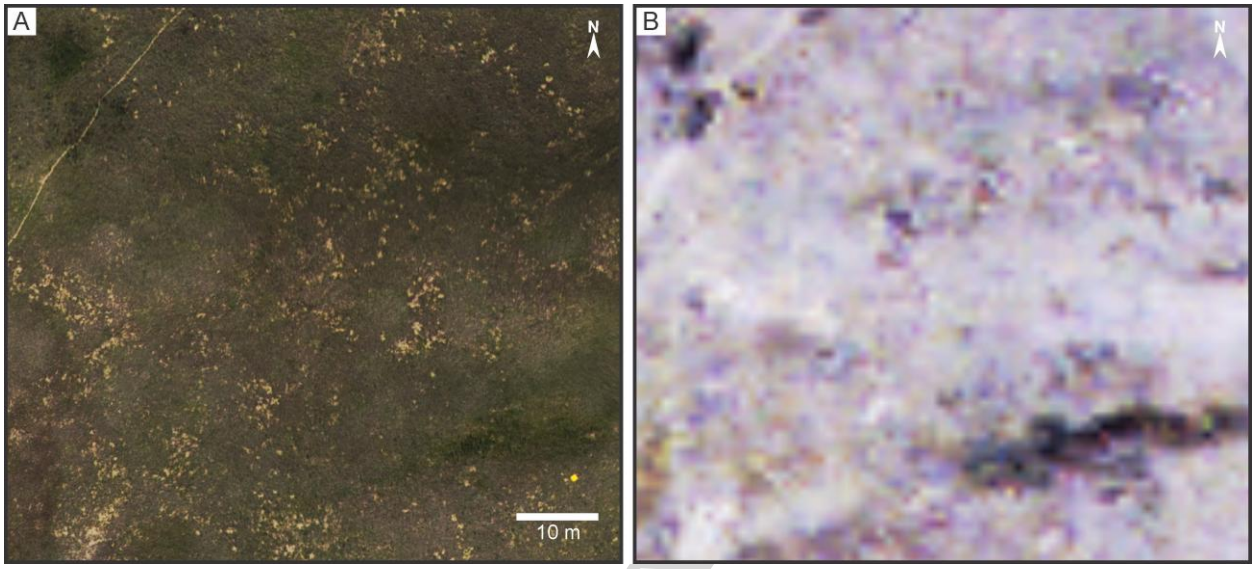

Fig. 9